Chapter 4

Time domain analysis

4.1 Introduction

In the past 20 years, the wind-excited response of structures to thunderstorm outflows has been studied by many researchers. Choi and Hidayat (2002) were the first to indicate that the commonly adopted method of gust response factor for atmospheric boundary layer winds underestimates the wind-excited response of structures due to thunderstorm outflow winds. They proposed the application of a running mean wind speed averaged over 60 seconds, instead of a constant mean averaged over 10 minutes to 1 hr, for the separation of the mean and turbulent component of wind speed. Following this indication, several recommendations were made for the averaging period and technique of the running mean wind speed(Chen and Letchford, 2005, 2006; Holmes et al., 2008; Lombardo et al., 2014; Solari et al., 2015a; Tubino and Solari, 2020). However, since the turbulent component of the wind speed obtained as a residue of the running mean separation is also nonstationary, the frequency domain approach applied for atmospheric boundary layer winds could not be directly adopted. As a result, different time domain, frequency domain, and time-frequency domain methods for the calculation of wind-excited response due to thunderstorm outflows were proposed by researchers.

Chen and Letchford (2004) applied time-domain analysis, to study the along-wind response of a tall building to downburst winds assuming a perfectly correlated wind field. Holmes et al. (2005) studied the along wind response of single degree of freedom structures to a recorded wind speed time history during a downburst using Duhamel's integral, to obtain the dynamic response factor which is the ratio between the equivalent static force and the maximum loading. Chen (2008) proposed a frequency domain approach to estimate the along-wind response of structures to transient, nonstationary winds by modeling the wind loads as the sum of deterministic time-varying mean and evolutionary random fluctuation. Kwon and Kareem (2009)

proposed the generalized gust front factor framework that encompasses the gust loading factor, a widely applied procedure for synoptic winds, under a single umbrella with the procedure for thunderstorm/downburst winds. Solari et al. (2015b) proposed the thunderstorm response spectrum method, a method analogous to the response spectrum in earthquake engineering, for a single degree of freedom systems using the numerous thunderstorm wind records collected by a network of anemometers. Working in the time-frequency domain, Roncallo and Solari (2020) proposed a new approach to the derivation of the evolutionary power spectral density (EPSD) function for the residual turbulent fluctuations of the downburst wind speed based on the hypothesis of a uniformly modulated process.

However, each of the studies considered several simplifying assumptions for the wind field and the wind load. Recent monitoring campaigns for the collection of thunderstorm wind data through a closely spaced network of anemometers and Lidar vertical profilers provided crucial input on the wind field property (Canepa et al., 2020; Huang et al., 2019; Repetto et al., 2017; Solari et al., 2020). On the other hand, it would be convenient to measure wind-and-structural response simultaneously during thunderstorm outflows, to compare the response calculated using the simplifying assumptions of wind load with the registered response.

In this chapter, the response of the monitored structure introduced in Chapter 2, during two real downburst records presented in Chapter 3, is calculated in the time domain adopting simplifying assumptions for the wind field and aerodynamic loading. The result is then compared with the registered response of the structure during the two downburst records to highlight the implication of the considered simplifying assumptions.

The procedure for the calculation of response in the time domain with a detailed explanation of the generation of the wind field, calculation of the aerodynamic load, and the dynamic response is presented in Section 4.2. The calculated response time history is compared with the registered response in Section 4.3. On the basis of the comparison, a second numerical analysis is made, adopting optimized aerodynamic coefficient, and the result is compared with the registered response in Section 4.4. Finally, conclusions are made and prospects for future research are recommended in Section 4.5.

4.2 Calculation of response in the time domain

In this section, the wind speed time history recorded during the two case studies of downbursts is used to calculate the wind load time history on the monitored structure. Then, the wind load time history is applied to the equation of motion of the monitored structure to obtain the response time history. The considered time history for wind load and response calculation is the most intense

part of the wind which is the 10-minute time interval centering the maximum instantaneous wind.

4.2.1 Wind field

In order to calculate the wind pressure and the total wind load acting on the structure, the wind speed time history at various heights is essential. However, since measurement of wind speed at various heights was not available, it had to be estimated from the reference time history of wind speed registered at the anemometric location, assuming suitable models for mean wind speed profile, turbulence intensity profile, and turbulence coherence.

Extending the model already introduced in Eqs 3.10 and 3.11 spatially, the wind field in the alongwind and crosswind direction can be calculated by:

$$\begin{aligned} u(z,t) &= \bar{u}(z,t) + u'(z,t) \\ &= \bar{u}(z,t)\left[1 + I_u(z,t)\tilde{u}'(z,t)\right] \end{aligned} \tag{4.1}$$

$$v(z,t) = v'(z,t) = \bar{u}(z,t) I_v(z,t)\tilde{v}'(z,t) \tag{4.2}$$

Thus, the vertical profile of the three components of the wind speed, namely, slowly varying mean wind speed, turbulence intensity, and the reduced fluctuating component must be modeled.

Time-varying mean wind speed profile

Few models are available for the vertical profile of mean wind speed during a downburst (Li et al., 2012; Oseguera and Bowles, 1988; Vicroy, 1991, 1992; Wood et al., 2001). For this research, the empirical formula derived by Wood et al. (2001) through a wind tunnel simulation has been used to calculate the slowly varying mean wind speed at various heights of the structure. The mean wind speed at height z from the ground, $\bar{u}(z,t)$, is given by

$$\bar{u}(z,t) = \bar{u}(h,t)\left(\frac{z}{h}\right)^{1/6} \frac{\left[1 - erf\left(0.7\frac{z}{\delta}\right)\right]}{\left[1 - erf\left(0.7\frac{h}{\delta}\right)\right]} \tag{4.3}$$

where $\bar{u}(h,t)$ is the mean wind speed registered by the anemometer; $\delta = 6Z_{\max}$ is the height at which the mean wind speed is $0.5u_{\max}$, $u_{\max}$ being the maximum mean wind speed in the vertical direction; $Z_{\max}$ is the height of the maximum wind speed; erf is the error function.

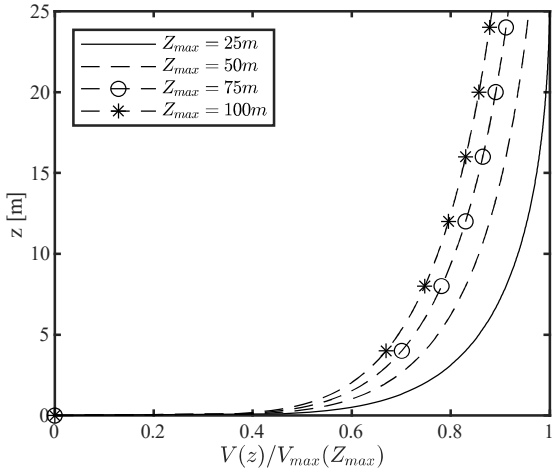

Fig. 4.1 Profile of mean wind speed

Applying this empirical formula, the vertical profile of the mean wind speed increases up to a certain height, $Z_{\max}$, attaining the maximum wind speed, $u_{\max}$, and decreases afterward, creating a nose shape profile. The height $Z_{\max}$ is an uncertain parameter that varies for different downburst events. Recent studies (Canepa et al., 2020) showed that the vertical profile of the mean wind speed is not nose-shaped throughout the period of the downburst, rather it varies in time, from nearly constant to nose-shaped and nearly logarithmic. However, for this research, the profile of the mean wind speed is considered constant in time but a range of values from 25 m to 100 m are considered for the value of $Z_{\max}$, to have vertical profiles of varying shapes. Fig. 4.1 shows the considered vertical profiles of mean wind speed normalized with respect to the maximum wind speed.

Turbulence intensity profile

A study of measurement of the wind speed at various heights ranging from 40 m to 250 m using a LiDAR profiler has shown that the turbulence intensity is not constant in the vertical direction and it varies in time (Canepa et al., 2020). However, the possibility of defining a model, for the vertical profile of turbulence intensity in thunderstorm winds is not yet studied. As a result, in this study, turbulence intensity is assumed to be constant in the vertical direction, equal to the turbulence intensity obtained at the anemometer location, so that $I_u(t,z) = I_u(t,h)$ and $I_v(t,z) = I_v(t,h)$.

Reduced fluctuating component

Previous studies have shown that the power spectral density (PSD) of the reduced fluctuating component of wind, $\tilde{u}'$ and $\tilde{v}'$, has similar properties with the PSD of the fluctuating component in the classical ABL winds (Chen and Letchford, 2004; Holmes et al., 2008; Kwon and Kareem, 2009; Lombardo et al., 2014; Solari et al., 2015a). However, the coherence of this reduced fluctuating component of wind in space is not sufficiently addressed. In previous studies, the coherence in space was assumed to be the same as the coherence of fluctuating components of wind speed in the atmospheric boundary layer (ABL) winds (Brusco et al., 2019; Solari, 2016; Solari et al., 2017). Although sufficient investigations have not been done on the coherence of wind fields during downbursts, researchers indicated that coherence models proposed for ABL winds might not be applicable to downburst outflows. In the present study, the coherence of the wind field in the vertical direction was considered to be an uncertain parameter. In particular, a wind field whose reduced fluctuating component is perfectly correlated (Case A) and a wind field whose reduced fluctuating component is partially correlated, with coherence in space similar to ABL winds (Case B), were considered in this research.

The assumption of a perfectly correlated wind field (Case A) can be interpreted as a case in which the reduced fluctuating component of wind speed is constant in the vertical direction and equals the reduced fluctuating component registered at the anemometric height. Thus, the time and height-dependent wind speed components $\tilde{u}'(z,t)$ and $\tilde{v}'(z,t)$ will be simplified as only time-dependent, $\tilde{u}'(h,t)$ and $\tilde{v}'(h,t)$. This case will give the ideal upper limit of the fluctuating component of wind. With this assumption, the wind field is given by:

$$\begin{aligned} u(z,t) &= \bar{u}(z,t) + u'(h,t) \\ &= \bar{u}(z,t)\left[1 + I_u(h,t)\tilde{u}'(h,t)\right] \end{aligned} \tag{4.4}$$

$$v(z,t) = v'(h,t) = \bar{u}(z,t) I_v(h,t) \tilde{v}'(h,t) \tag{4.5}$$

where the vertical variation is only due to the mean wind profile.

The assumption of a partially correlated wind field (Case B) considers the coherence in space of the reduced fluctuating component of the wind speed to be similar to the case of ABL winds. In addition, to avoid the numerical generation of cross-correlated time histories at various heights of the structure, the equivalent wind spectrum technique (EWST) is applied. This technique initially introduced in Solari (1988), was enhanced specifically for slender structures in Piccardo and Solari (1998). It substitutes the fluctuating wind field along the height of the

structure, $\tilde{u}'(z,t)$ and $\tilde{v}'(z,t)$, by equivalent fluctuating wind fields, $\tilde{u}'_{eq}(t)$ and $\tilde{v}'_{eq}(t)$. Note that $\tilde{u}'_{eq}(t)$ and $\tilde{v}'_{eq}(t)$ are not height dependent, which makes them identically coherent in space. The fluctuating time history of the wind speed registered at a reference location is converted into an equivalent fluctuating time history in such a way that the first modal force obtained by applying the equivalent wind load is equal to the first modal force obtained by the generation of cross-correlated time histories at various heights of the structure. The method works in the frequency domain, applying a frequency filter, C, to the Fourier-transformed fluctuating components of the wind speed registered at a reference location, $\hat{\tilde{u}}'(h,n)$ and $\hat{\tilde{v}}'(h,n)$, and converts them to equivalent fluctuating components, $\hat{\tilde{u}}'_{eq}(n,\delta_u)$ and $\hat{\tilde{v}}'_{eq}(n,\delta_v)$, expressed by

$$\hat{\tilde{u}}'_{eq}(n,\delta_u) = \hat{\tilde{u}}'(h,n)\sqrt{C(\delta_u n)} \tag{4.6}$$

$$\hat{\tilde{v}}'_{eq}(n,\delta_v) = \hat{\tilde{v}}'(h,n)\sqrt{C(\delta_v n)} \tag{4.7}$$

where $\hat{\tilde{u}}'(h,n)$ and $\hat{\tilde{v}}'(h,n)$ are the Fourier transforms of the reduced turbulent fluctuations $\tilde{u}'(h,t)$ and $\tilde{v}'(h,t)$ respectively; and h is the height of the anemometer.

The frequency filter C can be expressed by:

$$C(\eta) = \frac{1}{\eta} - \frac{1}{2\eta^2}\left(1 - e^{-2\eta}\right) \quad ;\eta > 0 \quad ;C(0) = 1 \tag{4.8}$$

where η is the argument of C. δ_u and δ_v are non-dimensional parameters expressing the dependence on the modal shape, the height of the structure, the exponential decay coefficients of coherence, and the mean wind speed at the reference height of the structure. They are expressed by

$$\delta_u = \frac{\kappa c_{uz} H}{\bar{u}_{\max}\left(Z_{eq}\right)} \qquad ,\delta_v = \frac{\kappa c_{vz} H}{\bar{u}_{\max}\left(Z_{eq}\right)} \tag{4.9}$$

where $\bar{u}_{\max}$ is the maximum value of the time-varying mean wind speed at the reference height of the structure; Z_{eq} is the reference height of the structure, considered to be $0.6H$; and c_{uz} and c_{vz} are the exponential decay coefficients of u' and v' respectively in the vertical direction. $c_{uz} = 10$ and $c_{vz} = 6$ are considered following the recommendation in Solari and Piccardo (2001) for ABL wind field. κ is a mode shape dependent parameter given by:

$$\kappa = \left(\frac{0.5}{\zeta_1 + 1}\right)^{0.55} \tag{4.10}$$

where ζ_1 is the power coefficient of the modal shape. For simplification, $\zeta_1 = 1.9$ corresponding to the first vibration mode shape in the Y-direction was considered.

The frequency filter, C, calculated for the two downburst events with their respective values of δ_u and δ_v is plotted in Fig. 4.2. It can be observed that the reduction in amplitude of turbulent wind is significant, close to 0.4, for frequency components near the first two modal frequencies of the structure ($n_{1,Y} = 0.75$ and $n_{1,X} = 0.85$).

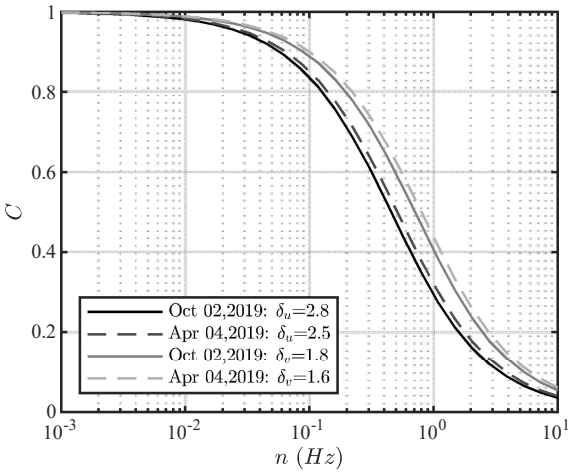

Fig. 4.2 Frequency filter function for the application of the EWST

The frequency filter in Fig. 4.2 was applied to the two reduced fluctuating components of wind speed, $\tilde{u}'(h,t)$ and $\tilde{v}'(h,t)$, following the deterministic procedure introduced in Solari (2016) and the equivalent fluctuating components, $\tilde{u}'_{eq}(t)$ and $\tilde{v}'_{eq}(t)$, were obtained, applying the inverse Fourier transformation to the equivalent fluctuating components, $\hat{\tilde{u}}'_{eq}(n,\delta_u)$ and $\hat{\tilde{v}}'_{eq}(n,\delta_v)$.

Finally, with the application of the equivalent wind spectrum technique, the equivalent wind field for Case B was obtained as

$$\begin{aligned} u_{eq}(z,t) &= \bar{u}(z,t) + u'_{eq}(z,t) \\ &= \bar{u}(z,t)\left[1 + I_u(h,t)\tilde{u}'_{eq}(t)\right] \end{aligned} \tag{4.11}$$

$$v_{eq}(z,t) = v'_{eq}(z,t) = \bar{u}(z,t) I_v(h,t)\tilde{v}'_{eq}(t) \tag{4.12}$$

4.2.2 Wind loading

Aerodynamic coefficients

An experiment to investigate the aerodynamic properties of the monitored structure was done in a conventional boundary layer wind tunnel by Orlando et al. (2023). Since the cross-section of the pole is not uniform and decreases with height, the experiment was done by realizing a 3-D model of the 16-sided polygon with scaled dimensions of the largest cross-section at the bottom of the pole and the smallest cross-section at the top of the pole. In addition, a separate experiment was done for the rectangular platform at the top of the structure. The attached ladder on one of the sides of the cross-section of the pole was also part of the experimentation. Detailed explanations of the wind tunnel study can be found in Orlando et al. (2023).

The applicability of aerodynamic coefficients obtained through the conventional boundary layer wind tunnel requires further examination. Wind tunnel investigation on circular cylinders under downburst-like outflows indicated that the location of the cylinders in downburst-like outflows plays a major role in the aerodynamics and the results in lift coefficients are different at the base and the top of the cylinders (Romanic et al., 2020). On the other hand, the rapid increase and decrease in wind speed, as well as the change in wind direction also results in further complexity to the problem because the aerodynamic coefficients are in general dependent on the angle of attack and Reynolds number. Apart from uncertainties arising from the nature of downburst outflows, the geometry of the monitored structure also calls for further attention due to, the presence of two platforms at the intermediate and at the top level of the structure, non-prismatic tapered geometry, and the attached ladder on one of the sides of the cylinder.

In this study, aerodynamic coefficients, C_d and C_l, obtained through wind tunnel experiments for the large and small cross-sections as well as the rectangular platform were used to obtain time-varying aerodynamic coefficients, $C_d(t)$ and $C_l(t)$, depending on the angle of attack, $\bar{\beta}(t)$. Figs. 4.3 and 4.4 show the aerodynamic coefficients of the large section, small section, and rectangular platform corresponding to the time-varying angle of attack, in the two case studies of downbursts. Furthermore, aerodynamic coefficients of the pole that varies with time and height, $C_d(z,t)$ and $C_l(z,t)$, were obtained from $C_d(t)$ and $C_l(t)$ of the large and small section, through linear interpolation.

Aerodynamic loading

In section 4.2.1, the wind field along the height of the structure was defined considering the partial and perfect correlation of the wind field in the vertical direction. Assuming strip and quasi-steady

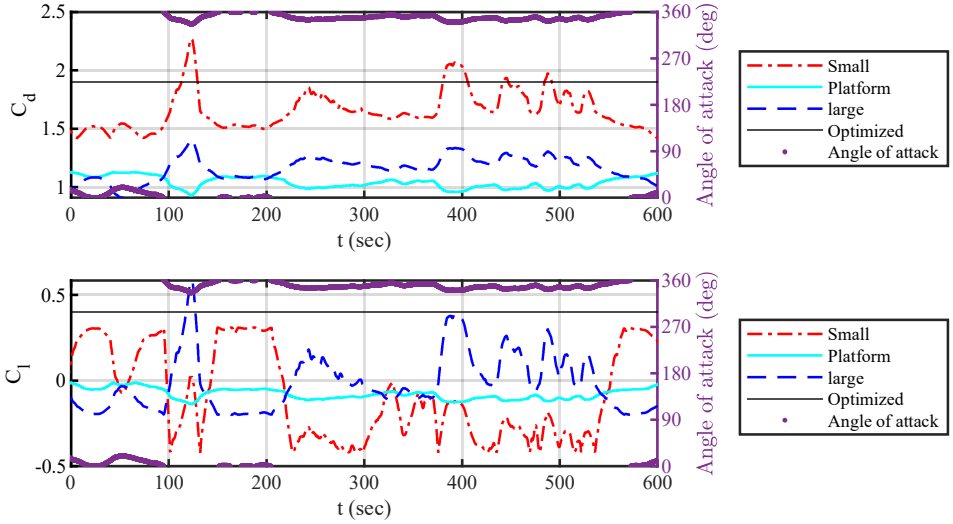

Fig. 4.3 Aerodynamic coefficients for the downburst on April 04, 2019

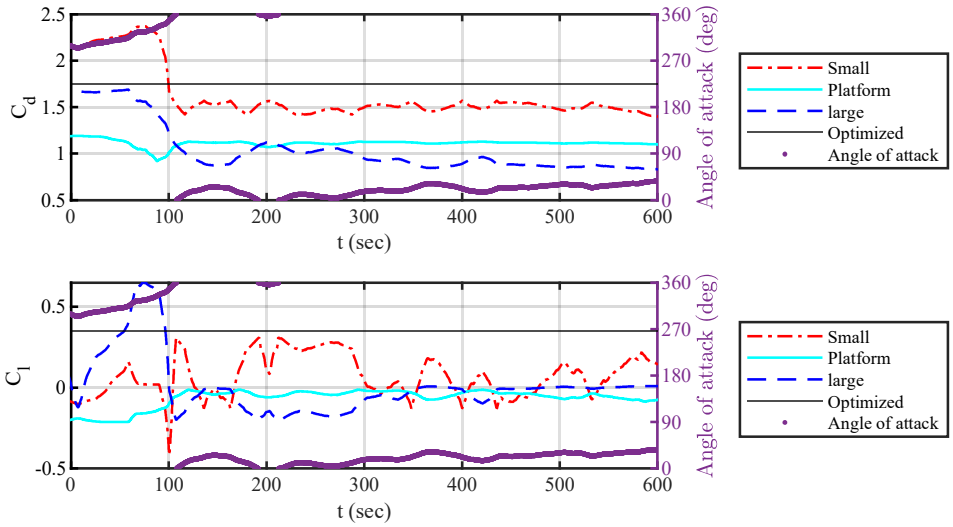

Fig. 4.4 Aerodynamic coefficients for the downburst on October 02, 2019

theory, and considering time and height-dependent aerodynamic coefficients (Section 4.2.2), the drag and lift forces were calculated, as follows

$$f_d(z,t) = \frac{1}{2}\rho b(z)U^2(z,t)C_d(z,t) \tag{4.13}$$

$$f_l(z,t) = \frac{1}{2}\rho b(z) U^2(z,t) C_l(z,t) \tag{4.14}$$

where $f_d(z,t)$ and $f_l(z,t)$ are the drag and lift forces respectively; $b(z)$ is the windward breadth of the structure; $c_d(z,t)$ is the drag coefficient; $c_l(z,t)$ is the lift coefficient; $U(z,t)$ is the resultant of the alongwind and crosswind speed given by Eq. 4.15 for the case of perfectly correlated wind field (Case A) and for the case of partially correlated wind filed field (Case B).

$$\begin{aligned} U(z,t) &= \sqrt{(u(z,t))^2 + (v(z,t))^2} \qquad CaseA \\ U(z,t) &= \sqrt{\left(u_{eq}(z,t)\right)^2 + \left(v_{eq}(z,t)\right)^2} \qquad CaseB \end{aligned} \tag{4.15}$$

Since the equation of motion will be solved in the principal bending directions of the structure, the drag and lift forces were projected on the principal axes X-Y (Fig. 4.5), obtaining the two orthogonal components given by

$$F_X(z,t) = F_d(z,t)\cos\left(44.5 - \gamma'(z,t)\right) + F_l(z,t)\sin\left(44.5 - \gamma'(z,t)\right) \tag{4.16}$$

$$F_Y(z,t) = -F_d(z,t)\sin\left(44.5 - \gamma'(z,t)\right) + F_l(z,t)\cos\left(44.5 - \gamma'(z,t)\right) \tag{4.17}$$

where γ' is the direction of the instantaneous wind velocity (Fig. 4.5) given by Eq. 4.18 for the case of perfectly correlated wind field (Case A), and for the case of partially correlated wind field (Case B):

$$\begin{aligned} \gamma'(z,t) &= \bar{\beta}(t) + a\tan 2\left[\frac{v'(h,t)}{\bar{u}(z,t) + u'(h,t)}\right] \quad (CaseA) \\ \gamma'(z,t) &= \bar{\beta}(t) + a\tan 2\left[\frac{v'_{eq}(t)}{\bar{u}(z,t) + u'_{eq}(t)}\right] \quad (CaseB) \end{aligned} \tag{4.18}$$

in which $\bar{\beta}(t)$ is the angle that the mean wind speed makes with the horizontal axis.

4.2.3 Dynamic response

The structure is modeled as a simplified linear cantilever beam clamped at the base. The equation of motion for multiple degree-of-freedom systems is

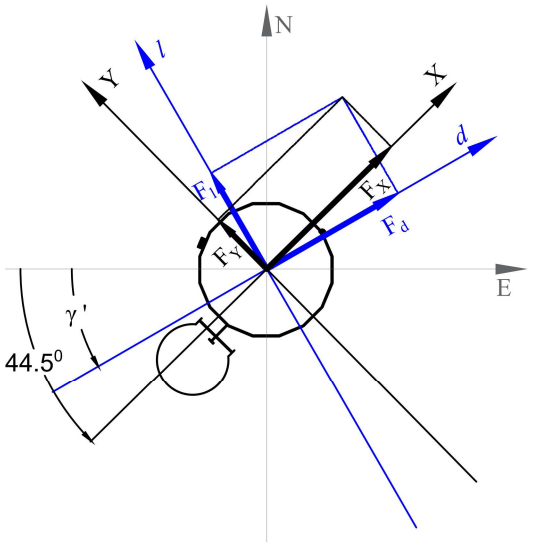

Fig. 4.5 Projection of aerodynamic force on the principal axes

$$\mathbf{M}\ddot{\mathbf{q}}(t)+\mathbf{C}(t)\dot{\mathbf{q}}(t)+\mathbf{K}\mathbf{q}(t)=\mathbf{F}(t) \tag{4.19}$$

where $\mathbf{M}$ is the mass matrix; $\mathbf{C}$ is the damping matrix; $\mathbf{K}$ is the stiffness matrix; $\mathbf{q}(t)$ is the displacement vector; and $\mathbf{F}(t)$ is the equivalent node force vector. Eq. 4.19 can be uncoupled as follows,

$$\ddot{p}_{n,i}(t)+2\xi_{n,i}\omega_{n,i}\dot{p}_{n,i}(t)+\omega_{n,i}^2 p_{n,i}(t)=\frac{1}{m_{n,i}}f_{n,i}(t) \tag{4.20}$$

where n is the mode; $p_{n,i}(t)$ is the n-th principal coordinate in the $i=X,Y$ direction; $\omega_{n,i}$ is the n-th circular frequency in the i direction ; $\xi_{n,i}$ is the n-th modal damping ratio in the i direction; $f_{n,i}(t)$ is generalized force; and $m_{n,i}$ is the n-th modal mass in the i direction.

The modal mass and the generalized force are given by

$$m_{n,i}=\sum_0^H m(z)\psi_{n,i}^2(z)dz \tag{4.21}$$

$$f_{n,i}(t)=\sum_0^H f_i(z,t)\psi_{n,i}(z)dz \tag{4.22}$$

where $\psi_{n,i}(z)$ is the n-th mode shape in the i direction; $m(z)$ is the mass per unit length; and $f_i(z,t)$ is the aerodynamic wind forces per unit length in the i-direction defined in Eqs. 4.16 and 4.17.

Since the damping ratio is uncertain, damping ratio $\xi_{n,i}$ of 0.2%, 0.5%, and 1% were considered for each mode, and aeroelasticity has been neglected.

The dynamic response is intended to be evaluated for the 10 minutes wind speed time history with the maximum instantaneous wind speed at the center. However, to consider the effect of initial conditions, the previous 2 minutes' wind time history was also considered. In addition, a cosine window function was applied to the 1st 1- minute wind loading time history to avoid the effect of an initial load. The application of this windowing function resulted in a wind load that starts from zero and reaches its registered intensity after one minute. The equation of motion was solved in the time domain using the state space method at a time step of 0.1 seconds to obtain the principal coordinates.

The displacement of the structure at any height, z, can be obtained from the principal coordinate as

$$q_i(z,t) = \sum_n \psi_{n,i}(z) p_{n,i}(t) \tag{4.23}$$

Since only the first two modes that are single curvature bending modes in the two orthogonal principal directions, X and Y, are considered, Eq. 4.23 reduces to:

$$q_i(z,t) = \psi_{1,i}(z) p_{1,i}(t) \tag{4.24}$$

In wind engineering, it is common to present the dynamic response in the alongwind and crosswind direction instead of the principal axes of bending. Thus, the calculated time history of response in the X and Y directions was projected on the time-varying alongwind and crosswind directions, x and y, as:

$$q_x(z,t) = q_X(z,t)\cos\left(44.5 - \bar{\beta}(t)\right) - q_Y(z,t)\sin\left(44.5 - \bar{\beta}(t)\right); \tag{4.25}$$

$$q_y(z,t) = q_X(z,t)\sin\left(44.5 - \bar{\beta}(t)\right) + q_Y(z,t)\cos\left(44.5 - \bar{\beta}(t)\right); \tag{4.26}$$

4.2.4 Results of the time domain integration

The response of the structure during the two case studies of downbursts was calculated using the 10 minutes registered wind speed time history during these events. Although many parameters have been estimated by means of full-scale monitoring and wind tunnel tests, time domain

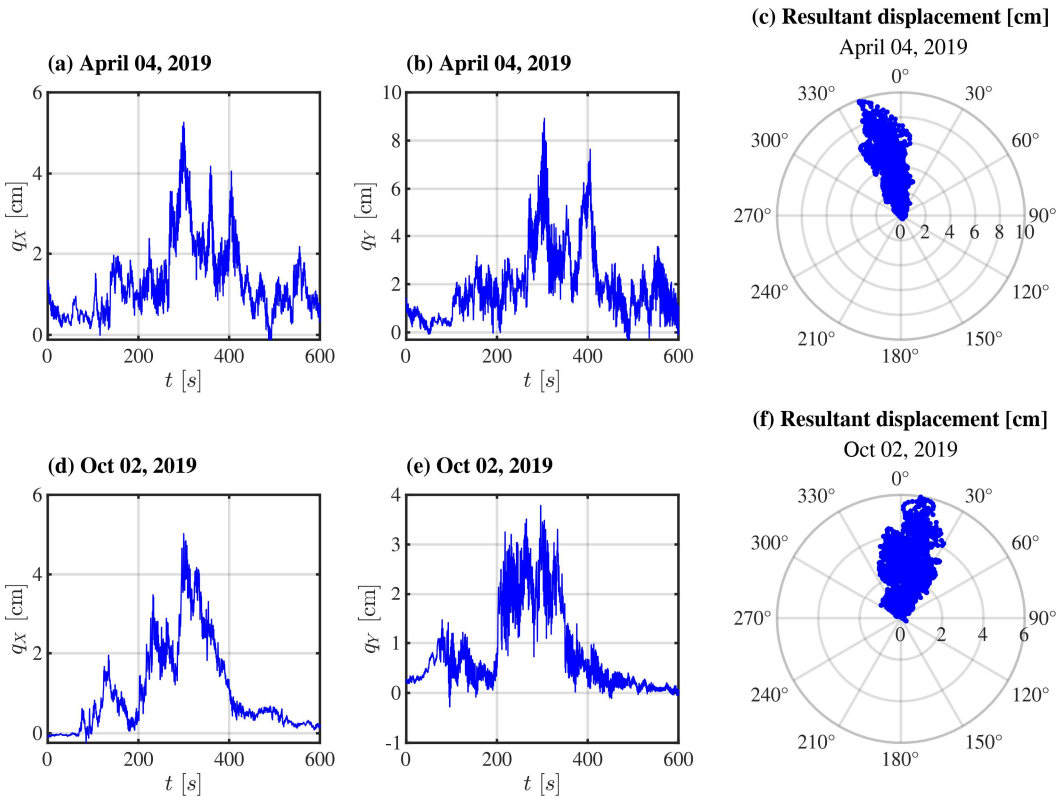

Fig. 4.6 Results of time domain analysis with the assumption of a partially correlated wind field, $Z_{max} = 25m$, experimental aerodynamic coefficients, and $\xi = 0.5\%$

analysis is still affected by unpredictable parameters. The main sources of uncertainty in this calculation are the vertical profile of the mean wind speed, the turbulence intensity and the coherence of the wind field, the transient aerodynamic coefficients, and the damping ratios of the structure.

The uncertainty of the vertical profile of mean wind speed was addressed by varying the parameter, Z_{max} assuming the values $Z_{max} = 25, 50, 75, 100\ m$ in the adopted empirical formula of mean wind speed profile (Eq. 4.3). This assumption affects both the static and dynamic response of the structure by a similar scale.

The uncertainties of turbulence intensity and coherence of wind field in the vertical direction affect the dynamic response. In the present research, turbulence intensity is assumed as constant in height and equal to the one measured at the top of the structure; the variability of the coherence is addressed by considering two cases of perfectly and partially correlated wind fields as described in Section 4.2.1.

Table 4.1 Percentage decrease in response relative to results with the assumption of $Z_{max} = 25$ m

Direction	Z_{max} [meters]		
	100	50	75
X	6.4%	5.8%	4.4%
Y	6.1%	5.5%	4.2%

Table 4.2 Dynamic amplification due to the mean wind speed

Event	Direction	Damping		
		0.2%	0.5%	1%
Apr 04, 2019	Alongwind	1.0189	1.0098	1.0074
	Crosswind	1.0594	1.0310	1.0174
Oct 02, 2019	Alongwind	1.0122	1.0102	1.0085
	Crosswind	1.0449	1.0241	1.0175

The uncertainty of aerodynamic coefficients is addressed by adopting two different approaches. Firstly, the dynamic response is calculated using experimental time-varying drag and lift coefficients according to the time-varying angle of attack, $\bar{\beta}$ (Figs. 4.3 and 4.4). Later, optimized aerodynamic coefficients are retrieved from the comparison between the calculated and measured responses.

The uncertainty of the damping ratio affects both the structural and aerodynamic damping. Aerodynamic damping was neglected as its prevalence in short-lived transient events is not widely studied. The structural damping ratio was varied as 0.2%, 0.5%, 1%. Generally, the damping ratio highly affects the dynamic response.

As an example, Fig. 4.6 shows the principal coordinate of displacement in the X and Y directions, and the polar plot of the resultant principal coordinate of displacements for the two case studies of the downbursts calculated with the assumption of $Z_{max} = 25\ m$, partially correlated wind field, experimental aerodynamic coefficients and structural damping ratio $\xi_1 = 0.5\%$.

4.3 Comparison of registered and calculated response

The displacement at the top of the structure in the alongwind and crosswind directions is selected to be the basis of comparison for the calculated and registered response. The top displacement time history in the alongwind and crosswind direction is calculated as explained in Section 4.2. The registered strain time histories during the two case studies of downbursts were analyzed

to obtain the top displacement time history, which will be referred to as the registered top displacement time history, in subsequent sections.

The comparison between the calculated and registered time history of top displacement is made for the mean and fluctuating part of the top displacement separately in the following subsections.

The time-varying mean wind speeds for the case studies of downbursts in this research were extracted using a 30-second moving window (Section 3.3.2). Similarly, the mean top displacement was extracted from the time history of the top displacement by calculating the running mean over 30 seconds for both the calculated and registered response. Thus, the mean top displacement is also time-varying. The fluctuating top displacement was then obtained by subtracting the time-varying mean from the total displacement.

4.3.1 Mean response

Since the mean wind speed is time-varying, the possibility of having a dynamic amplification due to the mean wind speed was checked. The dynamic amplification was calculated as the ratio of the dynamic and static response due to the mean wind speed. Table 4.2 shows the maximum dynamic amplification due to the mean wind speed obtained in the alongwind and crosswind directions. It can be concluded that the dynamic amplification due to the mean wind speed is negligible for all the assumed cases of damping ratios.

The effect of the variability of Z_{max} on the response of the structure has been evaluated. From Fig. 4.1, it can be observed that the total wind load decreases as Z_{max} increases from 25 m to 100 m. As a result the total response also decreases with an increase in Z_{max}. The significance of this uncertain parameter is evaluated by calculating the percentage decrease in the response of the structure relative to the response obtained with $Z_{max} = 25m$. The results, summarized in Table 4.1, show that the mean displacement of the structure, calculated through time domain integration, is not significantly affected by the assumption of Z_{max} different from 25 m.

On the basis of these discussions, the comparison between registered and calculated mean top displacement is presented for the case where Z_{max} is 25 m, experimental aerodynamic coefficients are considered (Figs. 4.3 and 4.4), and damping ratio $\xi = 0.5\%$. Fig. 4.7 shows the comparison between the time histories of the mean calculated and registered top displacement for the two downburst case studies. The correlation coefficient, r, between the time histories of the registered and calculated mean top displacement, is also shown at the top right corner of each sub-figure. In general, the time histories of the calculated and the registered mean top displacements in the alongwind direction have a similar trend. The maximum calculated mean displacement in the

alongwind direction is slightly higher than its registered counterpart, for both case studies of downbursts. However, the calculated and registered mean top displacements in the crosswind directions are not comparable in correlation and magnitude. Table 4.3 shows the percentage difference between the registered and calculated mean top displacements shown in Fig. 4.7, at the instant of maximum wind speed. Significant underestimation of the calculated mean crosswind response can be observed for both case studies of downbursts. In particular, the differing calculated and registered crosswind movement directions for the event of April 04 (Fig. 4.7(b)), indicate that this may be due to the uncertainty of the considered aerodynamic coefficients, especially the lift coefficients when used for the wind load calculation in thunderstorms.

Fig. 4.8 shows the comparison of the calculated and registered structural mean response direction during the two case studies of downbursts, calculated considering the experimental aerodynamic coefficients. The mean directional time history is qualitatively captured by the calculated response, with a shift of $\approx 19^\circ$ and 10° clockwise at the instant of maximum wind speed in the April 04 and October 02 events respectively. As the ratio between the drag and lift forces dictates the response direction relative to the wind speed direction, the deviation of the calculated response direction from the registered one confirms that the aerodynamic coefficients evaluated in stationary conditions are not able to capture the behavior of the structure during the two transient events. As can be observed in Figs. 4.3 and 4.4, the magnitude and sign of the lift coefficient vary notably for small changes in the angle of attack. These results call for further research on transient aerodynamics and the applicability of quasi-steady theory especially when strong directional variations are expected.

4.3.2 Peak response

Fig. 4.9 compares the time histories of the calculated and registered peak top displacement for the two downburst case studies for the case where the wind field is assumed to be partially correlated and the damping ratio is considered as 0.5%. Similar to the mean response, an overestimation of the calculated alongwind peak top displacement can be observed. In addition, the peak top displacement in the crosswind direction is underestimated for both case studies. The difference between the registered top peak displacement and the top peak displacement calculated with a range of assumptions of damping ratio and wind field correlation is summarized in Table 4.4. The values in brackets are the percentage differences between the registered and calculated peak top displacements. Positive values imply that the calculated peak top displacement is higher than its registered counterpart. It can be observed that while errors are below 20% in the alongwind direction, the calculated responses are significantly lower than the measured ones in almost all cases in the crosswind direction. The underestimation in the crosswind direction is up to 72.3%

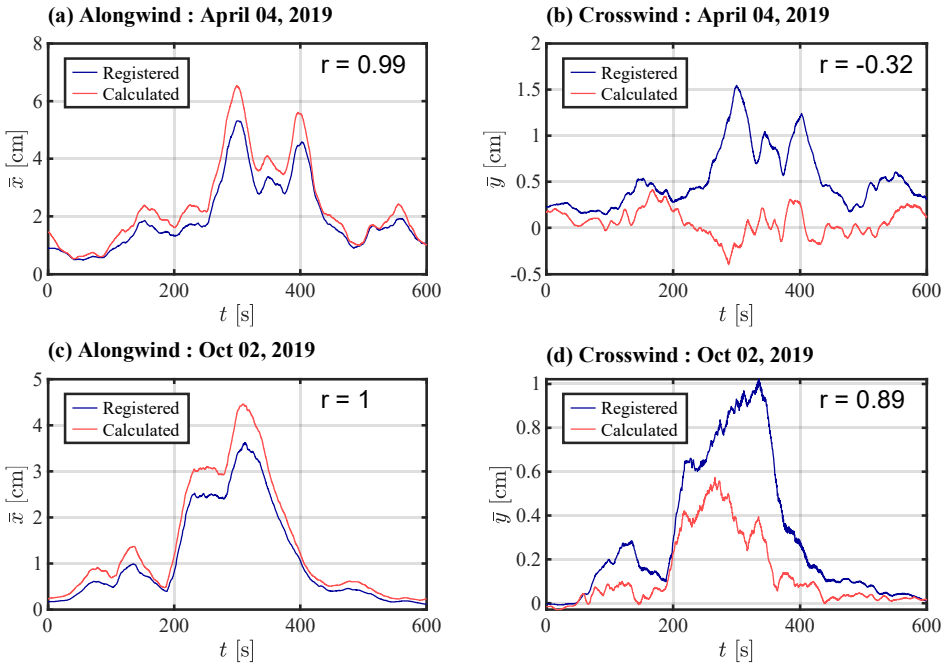

Fig. 4.7 Mean top displacement: registered vs. calculated with the assumption of $Z_{max} = 25\ m$, experimental aerodynamic coefficients, and $\xi = 0.5\%$

considering partial correlation and up to 51.5 % considering perfect correlation. Taking in mind the comparison shown in Section 4.3.1, it is not trivial to recognize and discuss the origin of the differences highlighted.

4.3.3 Root mean square of fluctuating response

The difference between the calculated and registered response is examined in further detail by comparing the root mean squared (RMS) of the top displacement fluctuation. The RMS of the top displacement fluctuation is in fact an essential parameter for comparing the fluctuating part of the response. The time-varying RMS of the top displacement fluctuation was obtained using a constant moving window of length 30 seconds. Figs. 4.10 and 4.11 show a comparison of the RMS of the calculated and registered fluctuating response. The comparison is done by calculating the moving RMS for results of different assumptions of damping ratio and wind field coherence because of their importance to the top displacement fluctuation. The correlation coefficient between the RMS of the calculated and registered top displacement fluctuation, r, is also shown in the legend of each subfigure. In general, it can be observed that the trend of the RMS of the top displacement fluctuation time history is well predicted in the alongwind

direction, although an underestimation of the dynamic response is shown for the October 02 event, even with perfect correlation and very low damping. The RMS of the response fluctuating is not satisfactorily predicted in the crosswind direction, where the numerical calculation was not able to predict the instant of maximum dynamic response.

Table 4.3 Percentage difference between the mean registered and calculated response with the assumption of a partially correlated wind field, $Z_{max} = 25m$, experimental aerodynamic coefficients, and $\xi = 0.5\%$

Event	Alongwind [%]	Crosswind [%]
April 04, 2019	20.1	-154.7
October 02, 2019	24.2	-85.9

Table 4.4 Difference between registered and calculated peak top displacement with $Z_{max} = 25m$ and experimental aerodynamic coefficients

Event	Damping ratio	Difference [cm]			
		Alongwind, x		Crosswind, y	
	[%]	Partial correlation	Perfect correlation	Partial correlation	Perfect correlation
Apr 04, 2019	0.2	0.7 (7.7%)	2.0 (19.4%)	-1.1 (-37.5%)	0.1 (3.3%)
	0.5	0.6 (6.3%)	1.7 (17.4%)	-1.6 (-61.0%)	-0.8 (-26.9%)
	1	0.3 (2.8%)	1.2 (12.1%)	-1.8 (-72.3%)	-1.4 (-51.5%)
Oct 02, 2019	0.2	0.2 (4.2%)	0.6 (10.2%)	-0.9 (-40.5%)	-0.3 (-11.4%)
	0.5	0.1 (1.5%)	0.6 (10.4%)	-1.2 (-60.5%)	-0.8 (-38.2%)
	1	0.1 (2.4%)	0.6 (9.1%)	-1.2 (-63.7%)	-0.9 (-43.2%)

4.4 Comparison of registered and calculated response based on optimized aerodynamic coefficients

In a previous study of the two case studies of downburst events, the trend of the mean wind speed squared time history and the alongwind and crosswind mean displacement time history was found to be similar. In addition, the correlation coefficients between the time history of the mean wind speed squared and the time history of the alongwind and crosswind mean displacement were also greater than 0.98 (Chapter 3). This result indicated that the mean alongwind and crosswind responses can be predicted with high accuracy if proper aerodynamic coefficients

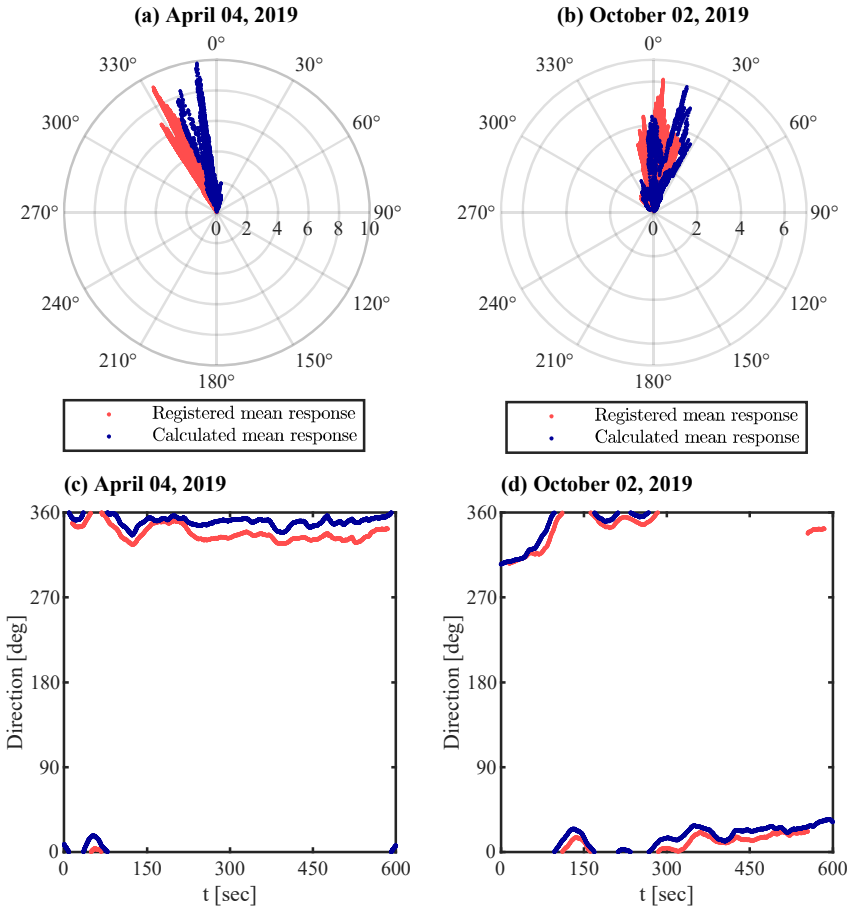

Fig. 4.8 Polar plot of the mean calculated (with experimental aerodynamic coefficients) and registered response trajectory ((a) and (b)), the time history of the mean calculated and registered response direction ((c) and (d))

are considered. However, in the previous Section significant differences between calculated and measured responses were shown in both the mean and the fluctuating part of the response. The uncertainties of the aerodynamic coefficients prevented a meaningful discussion on the uncertainties related to the coherence model and damping ratio.

In order to investigate the different sources of uncertainties in depth, further comparison of the calculated and registered peak response and RMS of the response fluctuation are proposed, after minimizing the uncertainties associated with the aerodynamic coefficients and the mean wind speed profile. To this aim, optimized aerodynamic coefficients are retrieved from measured mean response and then used to re-calculate numerically the top displacement of the structure

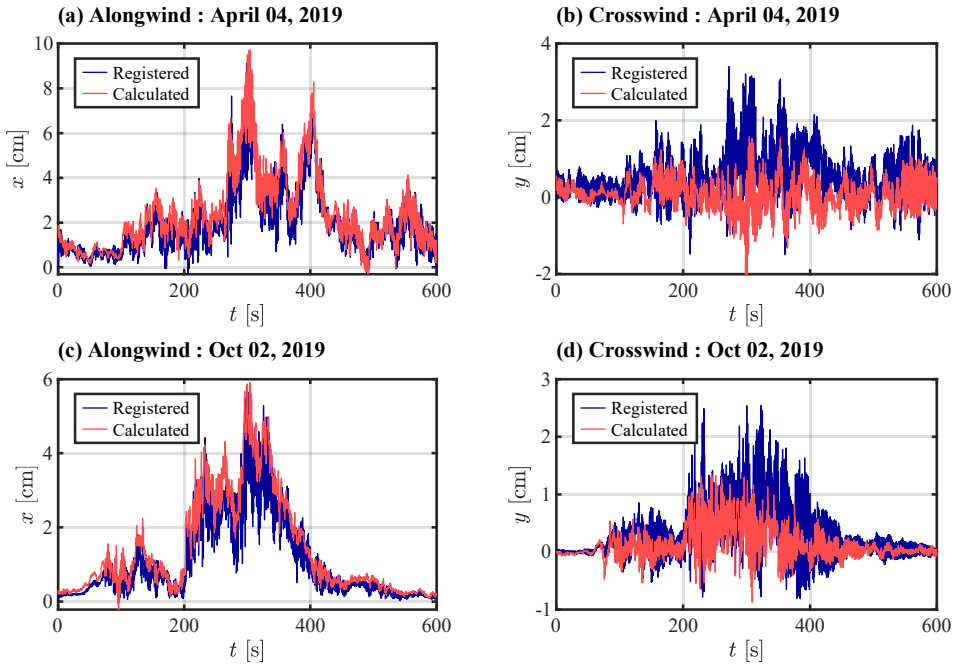

Fig. 4.9 Peak top displacement: registered vs. calculated with the assumption of a partially correlated wind field, $Z_{max} = 25\ m$, experimental aerodynamic coefficients, and $\xi = 0.5\%$

during the two considered events. This enabled the comparison of the registered and calculated peak response after the uncertainties due to aerodynamic coefficients and mean wind speed profile are removed.

4.4.1 Optimization of aerodynamic coefficients and mean response

In this section, the uncertainties in the aerodynamic coefficients and mean wind speed profile are minimized by finding equivalent aerodynamic coefficients, optimized in such a way that the calculated and registered mean responses of the structure are approximately similar.

With this objective, optimized aerodynamic coefficients that are constant in time and height were found for both downburst case studies. The optimization process is described in Table 4.5 and the resulting equivalent drag and lift coefficients are presented in Table 4.6 and reported as constant lines in Figs. 4.3 and 4.4. It can be observed that they are higher than the ones obtained from wind tunnel experiments.

The time-varying mean top displacement was calculated again using the optimized aerodynamic coefficients, which are constant in time, following the procedure in Section 4.2. The result

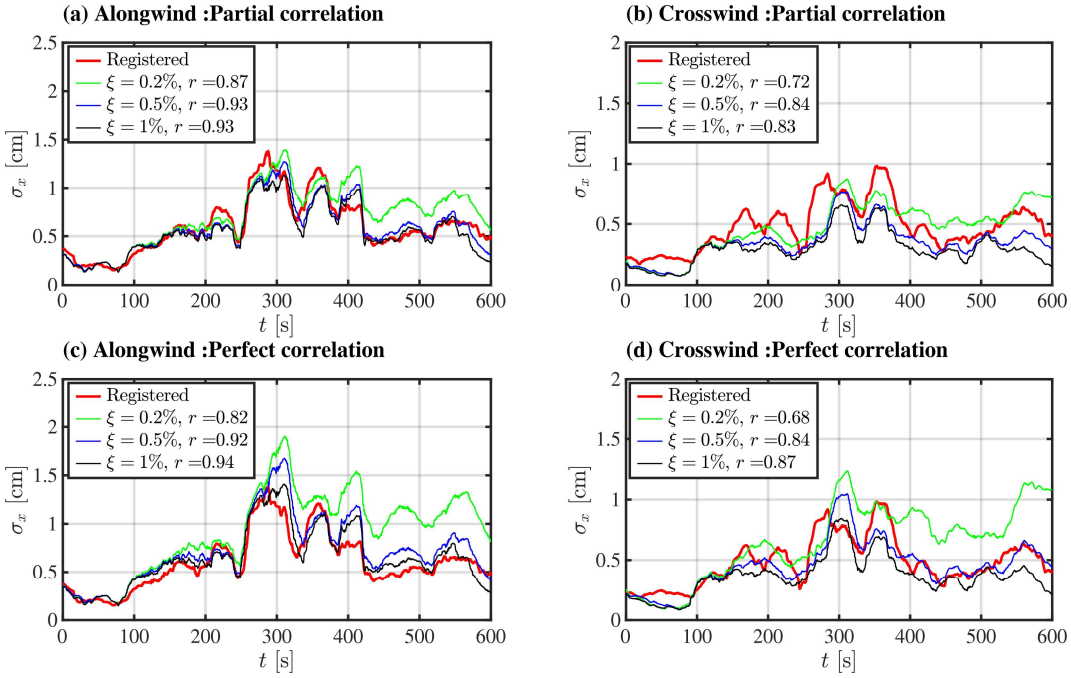

Fig. 4.10 RMS of the registered and calculated fluctuating top displacement with the assumption of $Z_{max} = 25\ m$ and experimental aerodynamic coefficients for the downburst event of April 04, 2019

Table 4.5 Procedure for calculating optimized aerodynamic coefficients

Step	Operation
1	Assume a combination of drag and lift coefficient from the range of values obtained in the wind tunnel testing.
2	Calculate the aerodynamic force using the assumed coefficients and obtain the displacement at the top of the structure in the two principal directions of the structure through time domain analysis.
3	Calculate the time-varying mean displacement at the top of the structure from the results obtained in step 2 using a constant moving window of length 30 seconds.
4	Calculate the time-varying displacement at the top of the structure using the registered strains, following the procedure in section 4.4, and extract the time-varying mean following a similar procedure as step 3.
5	Compare the time-varying mean displacement at the top of the structure obtained through time domain analysis with the one obtained from strain registrations. Quantify the similarity between the two results as a mean square error.
6	Repeat steps 1 to 5 for all combinations of drag and lift coefficients in the range and extract the combination that resulted in the smallest mean square error.

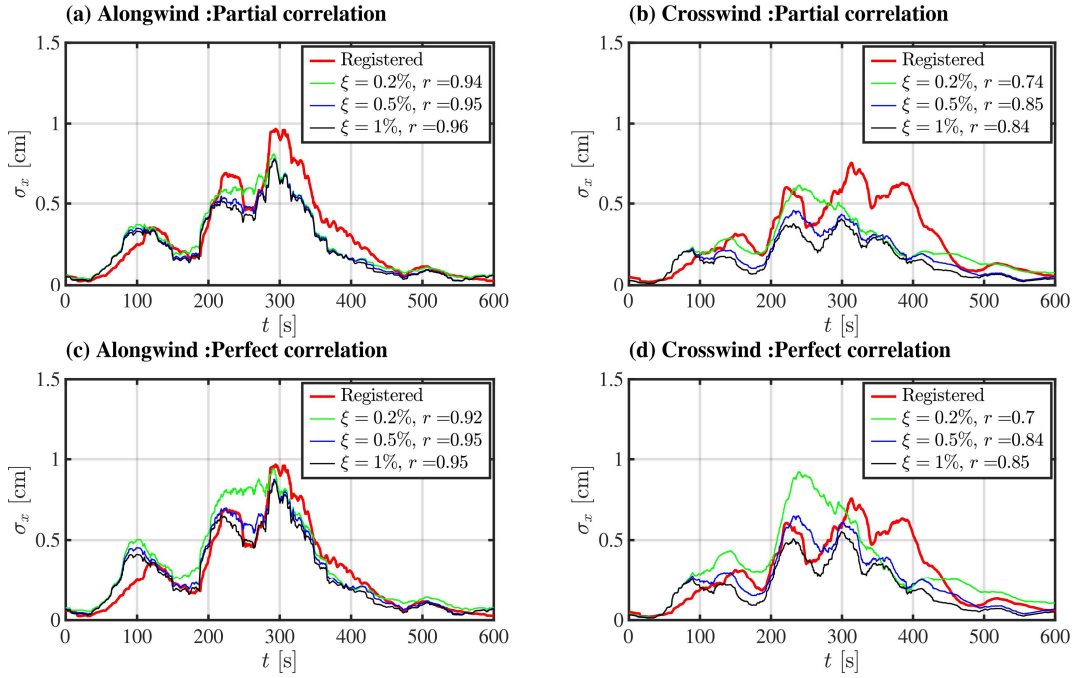

Fig. 4.11 RMS of the registered and calculated fluctuating top displacement with the assumption of $Z_{max} = 25\ m$ and experimental aerodynamic coefficients for the downburst event of October 02, 2019

Table 4.6 Optimized aerodynamic coefficients

Event	C_d	C_l
April 04, 2019	1.90	0.40
October 02, 2019	1.75	0.35

is compared with the registered time-varying mean top displacement in Fig. 4.12. The correlation coefficient between the registered and calculated mean response time histories, r, is also shown at the top right corner of each sub-figure. It can be observed that the time histories of the calculated and the registered mean top displacements are highly correlated, and their magnitude is approximately similar. Table 4.7 shows the percentage difference between the registered and calculated mean top displacement shown in Fig. 4.12, at the instant of maximum wind speed. In all cases, the percentage difference between the calculated and registered time-varying mean top displacement, at the instant of maximum wind speed, is lower than 6%.

Fig. 4.13 shows the comparison of the calculated and registered structural mean response direction during the two case studies of downbursts, calculated considering the optimized aerodynamic coefficients. As the ratio between the drag and lift forces dictates the response direction relative to the wind speed direction, the similarity between the calculated and registered

response direction confirms that the considered optimized aerodynamic coefficients are able to capture the behavior of the structure during the two events.

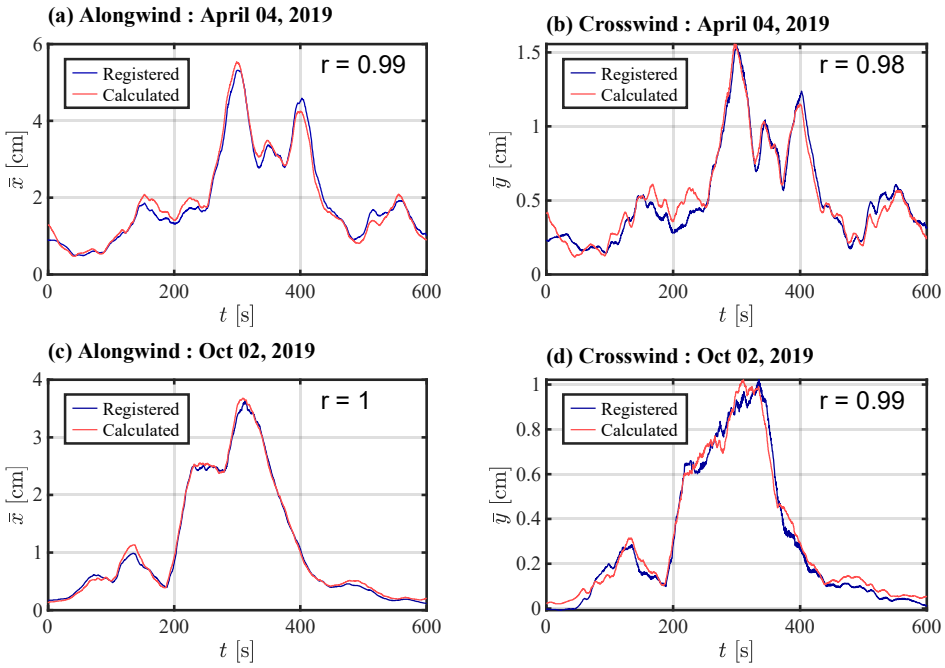

Fig. 4.12 Mean top displacement: registered vs. calculated with the assumption of a partially correlated wind field, $Z_{max} = 25m$, optimized aerodynamic coefficients, and $\xi = 0.5\%$

Table 4.7 Percentage difference between the mean registered and calculated response with the assumption of a partially correlated wind field, $Z_{max} = 25\ m$, optimized aerodynamic coefficients, and $\xi = 0.5\%$

Event	Alongwind [%]	Crosswind [%]
April 04, 2019	3.6	-1.2
October 02, 2019	5.2	4.9

4.4.2 Peak response

Since the calculated and registered mean displacements are now approximately similar, uncertainties due to the vertical profile of mean wind speed and aerodynamic coefficients are compensated by the optimized aerodynamic coefficients, and a comparison of the peak responses can be made.

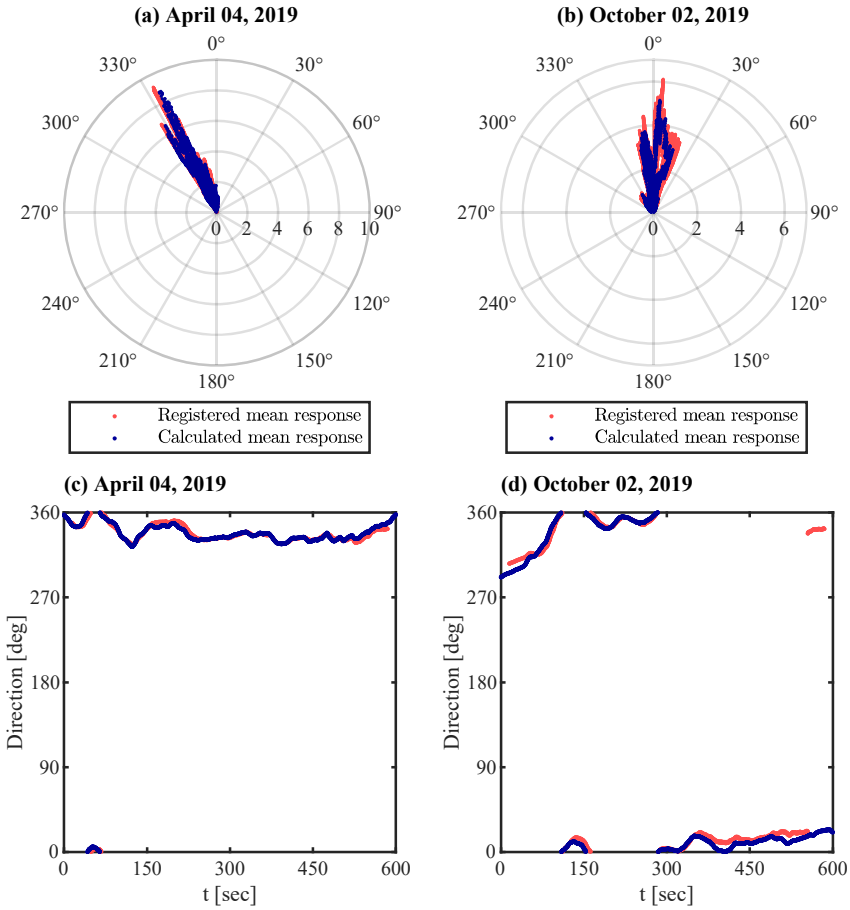

Fig. 4.13 Polar plot of the mean calculated (with optimized aerodynamic coefficients) and registered response trajectory ((a) and (b)), the time history of the mean calculated and registered response direction ((c) and (d))

Fig. 4.14 shows the top displacements calculated using the optimized aerodynamic coefficients and the registered top displacement, for the case where the wind field is assumed to be partially correlated and the damping ratio is considered as 0.5%. Since the absence of dynamic amplification due to the time-varying mean wind speed is proved, the difference between the peak and the mean response, which is the fluctuating part of the response, is mainly the result of the resonance between the modal vibration of the structure and the turbulent wind. This fluctuating response is highly dictated by the frequency content of the turbulent wind and the damping ratio of the structure. Thus comparison of the peak and fluctuating responses should be made considering the uncertainty of the coherence of the wind field and structural damping ratio. The difference between the registered top peak displacement and the top peak displace-

ment calculated with a range of assumptions of damping ratio and wind field correlation is summarized in Table 4.8. The values in brackets are the percentage differences between the registered and calculated peak top displacements. Positive values imply that the calculated peak top displacement is higher than its registered counterpart. In most of the considered assumptions, the peak alongwind displacement is underestimated by the numerical calculation even with the assumption of a perfectly correlated wind field and a damping ratio as low as 0.2% for both events. The underestimation decreases with the assumption of a perfectly correlated wind field and low damping ratio. The comparison for the event on October 02, 2019, showed that the peak response is underestimated both in the alongwind and crosswind direction regardless of the assumption of damping and correlation of wind field. Note that the event on April 04 had a background ABL wind before the occurrence of the sudden increase in wind speed while the event on October 02 occurred with no evident ABL wind. In general, the assumption of partially correlated wind with a correlation of the reduced fluctuating component similar to ABL wind underestimated both the alongwind and crosswind response except for one considered case. The case of perfect correlation was expected to give the upper bound of the response; however, it was exceeded by the registered response in most of the considered cases. The reason for the gap between the calculated and registered response fluctuations is still an open question. However, it may be attributed to the possibility of underestimation of turbulence through the assumption of constant turbulence intensity in the vertical direction. The turbulence intensity at various heights of the structure was assumed to be equal to the turbulence intensity registered at the anemometric location while in reality, the turbulence intensity at various heights of the structure may be higher than the intensity at the anemometric location.

Table 4.8 Difference between registered and calculated peak top displacement with $Z_{max} = 25m$ and optimized aerodynamic coefficients

Event	Damping ratio	Difference [cm]			
		Alongwind, x		Crosswind, y	
	[%]	Partial correlation	Perfect correlation	Partial correlation	Perfect correlation
Apr 04, 2019	0.2	-0.6 (-6.7%)	0.4 (4.5%)	0.2 (5.9%)	0.9 (23.3%)
	0.5	-0.9 (-9.9%)	-0.0 (-0.1%)	-0.0 (-1%)	0.6 (14%)
	1	-1.1 (-12.9%)	-0.4 (-4.4%)	-0.2 (-5.5%)	0.3 (7.4%)
Oct 02, 2019	0.2	-0.8 (-14.4%)	-0.5 (-8.4%)	-0.5 (-22%)	-0.1 (-4.5%)
	0.5	-0.9 (-17.9%)	-0.5 (-9.1%)	-0.7 (-30.1%)	-0.4 (-16.5%)
	1	-0.9 (-16.3%)	-0.6 (-10.6%)	-0.7 (-30.7%)	-0.4 (-17.5%)

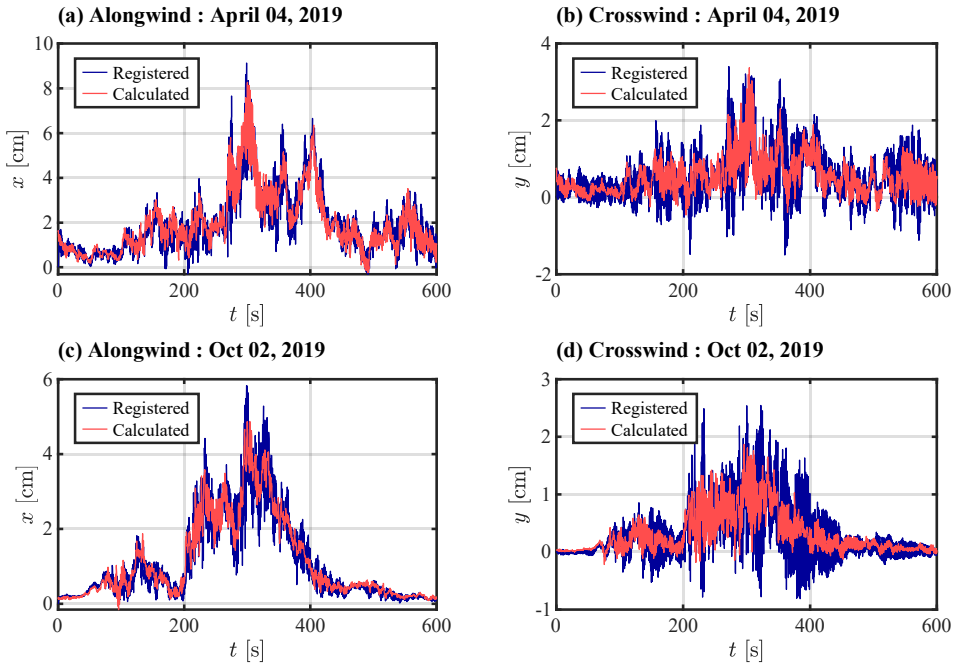

Fig. 4.14 Peak top displacement: registered vs. calculated with the assumption of a partially correlated wind field, $Z_{max} = 25m$, optimized aerodynamic coefficients, and $\xi = 0.5\%$

4.4.3 Root mean square of fluctuating response

In Figs. 4.15 and 4.16, the RMS of the top displacement fluctuation, calculated using the optimized aerodynamic coefficients with the assumption of different damping ratios and wind field correlations are compared with the RMS of the registered top displacement fluctuation. The correlation coefficient between the RMS of the calculated and registered top displacement fluctuation, r, is also shown in the legend of each subfigure.

For the event on April 04, the RMS of top displacement calculated with the assumption of partially correlated wind speed is underestimated while closer results are obtained for the case where a perfect correlation is assumed. For the event on October 02, the RMS of top displacement is underestimated in all the considered assumptions of damping ratio and wind field correlation. The underestimation is more pronounced in the second part of the time history, after the peak response. Comparing the two events, the event on April 04 that had a background ABL wind prior to the occurrence of a ramp-up in wind speed shows better predictability of the peak response and its fluctuation. In addition, observing the correlation coefficient, the RMS of the calculated response time history with a damping ratio of 0.2% is less correlated with the

RMS of the registered response time history, indicating that the damping ratio of the structure might not be as low as 0.2%.

Although the damping ratio has always been known to affect the dynamic amplification of response, the proper modeling of the correlation of wind fields is shown to be a factor that plays a significant role in the estimation of the dynamic response of the structure.

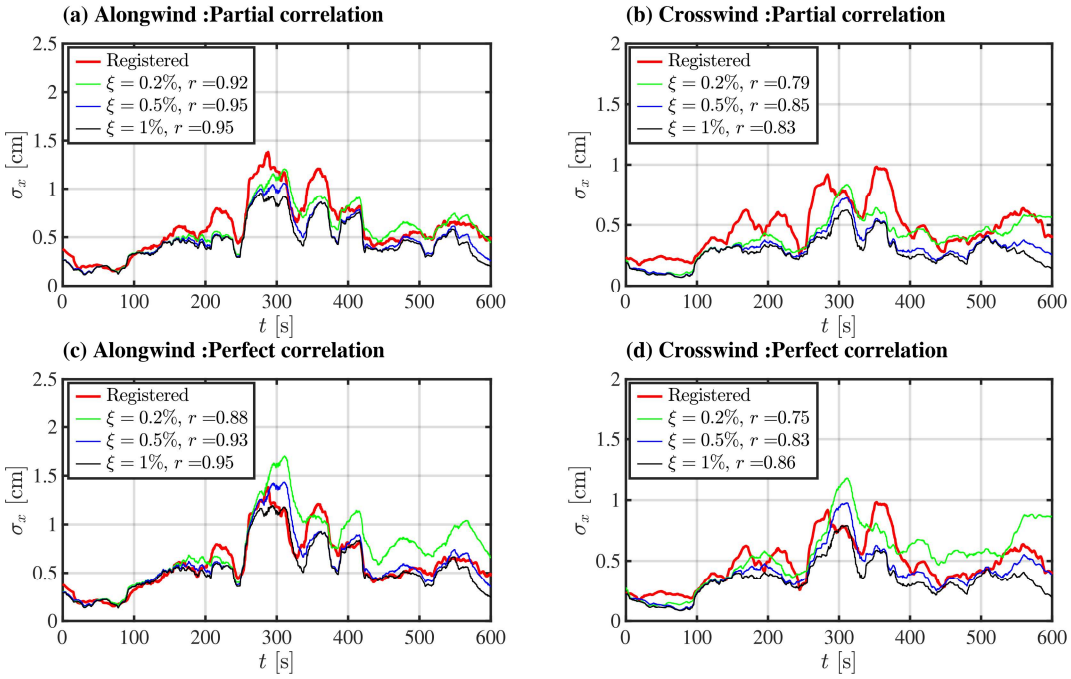

Fig. 4.15 RMS of the registered and calculated fluctuating top displacement with the assumption of $Z_{max} = 25m$ and optimized aerodynamic coefficients for the downburst event of April 04, 2019

4.5 Conclusion

The dynamic response of a slender light structure during two case studies of downburst winds was calculated using the registered time history of wind speed by the anemometer mounted on the structure. The calculation considered the uncertainty of wind field parameters, such as mean wind speed profile, turbulence intensity, and coherence, as well as structural parameters, such as the aerodynamic coefficients and damping ratio. The result is compared with the structure's response registered by the structural response monitoring system. The main conclusions of the study are as follows.

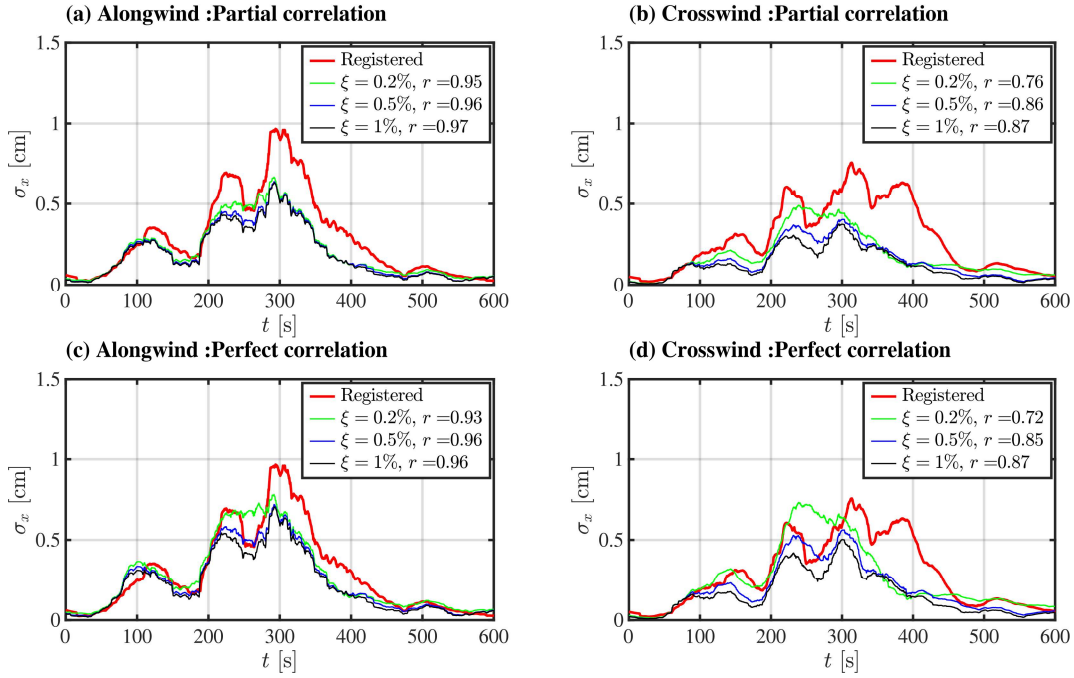

Fig. 4.16 RMS of the registered and calculated fluctuating top displacement with the assumption of $Z_{max} = 25m$ and optimized aerodynamic coefficients for the downburst event of October 02, 2019

- From the numerical analysis, the dynamic amplification due to the time-varying mean wind speed averaged over a 30-second moving window was negligible for all the assumed cases of damping ratios.
- The effect of the mean wind speed profile parameter Z_{max} on the response was small, at least for the current slender structure.
- The comparison of the calculated and registered mean response of the structure showed that the crosswind response was underestimated when aerodynamic coefficients obtained from wind tunnel testing are applied. The mismatch between the registered and calculated crosswind response and mean trajectories indicated that quasi-steady theory might not be applicable for transient events and the aerodynamic coefficients obtained from the wind tunnel testing might not be reliable for transient wind loading calculation.
- The comparison between the calculated and registered peak response of the structure obtained using the experimental aerodynamic coefficients showed that the calculated peak response is underestimated, especially in the crosswind direction. Comparisons between calculated and registered RMS of the top displacement are also shown. Uncertainties of

the aerodynamic behavior prevented a meaningful discussion about the dynamic response calculation.

- Optimized aerodynamic coefficients were retrieved from the comparison between the mean registered and calculated response to overcome uncertainties in aerodynamic behavior. The obtained equivalent time-invariant aerodynamic coefficients are larger than the experimental ones. Although the wind tunnel testing showed high sensitivity of the lift coefficient to the angle of attack, the comparison between the mean response of the structure calculated with optimized time-invariant aerodynamic coefficients and the registered response showed a good agreement in the structural response trajectory.

- The comparison between the calculated and registered peak response of the structure obtained using the optimized aerodynamic coefficients showed that the calculated peak response is mostly underestimated, even when the perfectly correlated wind field and the lowest damping value are considered. Such results make the assumption of space coherence similar to ABL wind and height-invariant turbulence intensity questionable.

- The peak response was found to be less predictable for the event in which the downburst had no background ABL wind. This observation should be further investigated using a wide set of downburst data.

- The RMS of the top displacement fluctuation, calculated with the assumption of different damping ratios and wind field correlations, was compared with the RMS of the registered top displacement fluctuation, showing a general underestimation even when optimized aerodynamic coefficients are used. Moreover, the RMS of the calculated response fluctuation with a damping ratio of 0.2% was found to be less correlated with the RMS of the registered response fluctuation, indicating that the damping ratio of the structure might not be as low.

In line with the results presented in Chapter 3, this research indicated that the mean response time history of the structure can be predicted with high accuracy if appropriate aerodynamic coefficients are considered. Such a result calls for further investigation of transient aerodynamic effects. However, the peak registered response was higher than predicted for most assumptions, even when optimized aerodynamic coefficients were adopted, indicating the need for further studies on the dynamic response to downbursts.

It is worth noting that the calculated alongwind response of the structure was comparable to the registered response with a percentage difference of not more than 25% in all cases. This has a positive implication for the analytical downburst response calculation approaches and

studies that are based on time domain analysis using similar assumptions for the wind field and aerodynamic load.

Although the structural damping ratio has always been known to affect the dynamic amplification of the response, transient aerodynamic coefficients, turbulence intensity, and coherence of downburst wind fields in space are shown to be parameters that need further attention.

References

Brusco, S., Lerzo, V., and Solari, G. (2019). Directional response of structures to thunderstorm outflows. *Meccanica*, 54(9):1281–1306.

Canepa, F., Burlando, M., and Solari, G. (2020). Vertical profile characteristics of thunderstorm outflows. *J. Wind Eng. Ind. Aerodyn.*, 206(August).

Chen, L. and Letchford, C. W. (2004). Parametric study on the along-wind response of the CAARC building to downbursts in the time domain. *J. Wind Eng. Ind. Aerodyn.*, 92(9):703–724.

Chen, L. and Letchford, C. W. (2005). Proper orthogonal decomposition of two vertical profiles of full-scale nonstationary downburst wind speeds. *J. Wind Eng. Ind. Aerodyn.*, 93(3):187–216.

Chen, L. and Letchford, C. W. (2006). Multi-scale correlation analyses of two lateral profiles of full-scale downburst wind speeds. *J. Wind Eng. Ind. Aerodyn.*, 94(9):675–696.

Chen, X. (2008). Analysis of Alongwind Tall Building Response to Transient Nonstationary Winds. *J. Struct. Eng.*, 134(5):782–791.

Choi, E. C. and Hidayat, F. A. (2002). Gust factors for thunderstorm and non-thunderstorm winds. *J. Wind Eng. Ind. Aerodyn.*, 90:1683–1696.

Holmes, J., Forristall, G., and Mcconochie, J. (2005). Dynamic response of structures to thunderstorm winds. *10th Am. Conf. Wind Eng. ACWE 2005*, (July 2017).

Holmes, J. D., Hangan, H. M., Schroeder, J. L., Letchford, C. W., and Orwig, K. D. (2008). A forensic study of the Lubbock-Reese downdraft of 2002. *Wind Struct. An Int. J.*, 11(2):137–152.

Huang, G., Jiang, Y., Peng, L., Solari, G., Liao, H., and Li, M. (2019). Characteristics of intense winds in mountain area based on field measurement: Focusing on thunderstorm winds. *J. Wind Eng. Ind. Aerodyn.*, 190:166–182.

Kwon, D. K. and Kareem, A. (2009). Gust-front factor: New framework for wind load effects on structures. *J. Struct. Eng.*, 135(6):717–732.

Li, C., Li, Q. S., Xiao, Y. Q., and Ou, J. P. (2012). A revised empirical model and CFD simulations for 3D axisymmetric steady-state flows of downbursts and impinging jets. *J. Wind Eng. Ind. Aerodyn.*, 102:48–60.

Lombardo, F. T., Smith, D. A., Schroeder, J. L., and Mehta, K. C. (2014). Thunderstorm characteristics of importance to wind engineering. *J. Wind Eng. Ind. Aerodyn.*, 125:121–132.

Orlando, A., Pagnini, L., and Pia Repetto, M. (2023). Wind tunnel tests of a hexadecagonal cylinder with imperfections and ancillaries: aerodynamic characterization and technical discussion. *Eng. Struct.*, 274(March 2022):115114.

Oseguera, R. M. and Bowles, R. L. (1988). A simple, analytic 3-dimensional downburst model based on boundary layer stagnation flow. Technical Report July.

Piccardo, G. and Solari, G. (1998). Generalized equivalent spectrum technique. *Wind Strutures*, 1(2):161–174.

Repetto, M. P., Burlando, M., Solari, G., De Gaetano, P., and Pizzo, M. (2017). Integrated tools for improving the resilience of seaports under extreme wind events. *Sustain. Cities Soc.*, 32:277–294.

Romanic, D., Nicolini, E., Hangan, H., Burlando, M., and Solari, G. (2020). A novel approach to scaling experimentally produced downburst-like impinging jet outflows. *J. Wind Eng. Ind. Aerodyn.*, 196(October 2019):104025.

Roncallo, L. and Solari, G. (2020). An evolutionary power spectral density model of thunderstorm outflows consistent with real-scale time-history records. *J. Wind Eng. Ind. Aerodyn.*, 203(April):104204.

Solari, G. (1988). Equivalent wind spectrum technique: Theory and applications. *J. Struct. Eng.*, 114(6):1303–1323.

Solari, G. (2016). Thunderstorm response spectrum technique: Theory and applications. *Eng. Struct.*, 108:28–46.

Solari, G., Burlando, M., De Gaetano, P., and Repetto, M. P. (2015a). Characteristics of thunderstorms relevant to the wind loading of structures. *Wind Struct. An Int. J.*, 20(6):763–791.

Solari, G., Burlando, M., and Repetto, M. P. (2020). Detection, simulation, modelling and loading of thunderstorm outflows to design wind-safer and cost-efficient structures. *J. Wind Eng. Ind. Aerodyn.*, 200(January):104142.

Solari, G., De Gaetano, P., and Repetto, M. P. (2015b). Thunderstorm response spectrum: Fundamentals and case study. *J. Wind Eng. Ind. Aerodyn.*, 143:62–77.

Solari, G. and Piccardo, G. (2001). Probabilistic 3-D turbulence modeling for gust buffeting of structures. *Probabilistic Eng. Mech.*, 16(1):73–86.

Solari, G., Rainisio, D., and De Gaetano, P. (2017). Hybrid simulation of thunderstorm outflows and wind-excited response of structures. *Meccanica*, 52:3197–3220.

Tubino, F. and Solari, G. (2020). Time varying mean extraction for stationary and nonstationary winds. *J. Wind Eng. Ind. Aerodyn.*, 203(October 2019):104187.

Vicroy, D. D. (1991). A simple, analytical, axisymmetric microburst model for downdraft estimation. *NASA Tech. Memo. No.104053*.

Vicroy, D. D. (1992). Assessment of microburst models for downdraft estimation. *J. Aircr.*, 29(6):1043–1048.

Wood, G. S., Kwok, K. C. S., Motteram, N. A., and Fletcher, D. F. (2001). Physical and numerical modelling of thunderstorm downbursts. *J. Wind Eng. Ind. Aerodyn.*, 89(2001):535–552.